Detailed Studies of the ATLAS Pixel Detectors

Clara Troncon [1]
Istituto Nazionale di Fisica Nucleare
Sezione di Milano
via Celoria 16, I-20133 Milano, Italy

Abstract

Results are reported from beam tests of prototype silicon pixel sensors and front-end electronics with analog readout developed for use in the ATLAS experiment at the Large Hadron Collider (LHC). Both irradiated and unirradiated assemblies were tested for charge collection, efficiency and position resolution measurements. These indicate that n^+ *in* n silicon pixel detectors with *p-spray* isolation can operate after irradiation to fluences of up to 10^{15} n_{eq}/cm^2 without significant degradation in performance. The depletion depth of irradiated sensors was measured and their behaviour in a magnetic field was studied. The Lorentz angle was found to decrease significantly after irradiation. Comparison between performance on spatial resolution obtained with digital or with analogical readout is also presented.

I. INTRODUCTION

The Atlas Collaboration at the LHC will construct a Pixel Detector in order to enhance its capability to perform pattern recognition in a high multiplicity environment and to provide high precision transverse impact parameter resolution for secondary vertex reconstruction and b-tagging. The Pixel Detector will consist of three barrel layers at radii 4.3, 10.1 and 13.2 cm and 5 × 2 disc structures which extend to ± 78 cm in the forward regions. The building block unit will be a module consisting of a silicon sensor *tile* with 16 front-end readout chips bump-bonded to it. The Pixel Detector will incorporate 2228 such modules with a total active area of 2.3 m^2. A challenging part of this project will be to construct a radiation hard detector able to survive in the harsh radiation environment of the LHC (design luminosity $\mathcal{L} = 10^{34} cm^{-2} s^{-1}$ leading to a fluence [2] of 10^{15} n_{eq}/cm^2 corresponding approximatively to 5 years of operation at the innermost barrel layer and to the experiment's expected lifetime of 10 years for the second barrel layer). A development program is being performed. Here we report test beam results on various sensor designs which support our baseline choice. A complete description of the project can be found in [1].

A. Detector Concept

Pixel Sensors. The Atlas pixel sensors consist of n^+ implants on a high resistivity n-bulk substrate [4]. This choice was made because it allows for operation in partially depleted mode after bulk inversion induced by radiation damage.

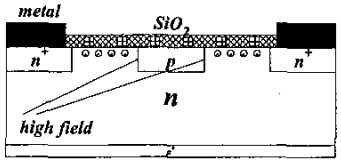

Figure 1: Schematic view of the implants in the p-stop insulation method. The charges inside the square boxes are fixed, the charges inside circles are free.

Since the inevitably existing positive charges present in the SiO_2 passivation layer and at the Si-SiO_2 interface induce a e^- accumulation layer that represents a conductive path shorting adjacent pixels, this choice required proper design of the isolation between n^+ pixels. Two isolation techniques were used in the prototype production: the *p-stop* [5], where a high dose p-implant surrounds the n-cell (Fig. 1) and the newly developed *p-spray* [6] technique, where a uniform medium dose p-implant covers the whole n-side and is over-compensated by the high dose of the pixel implants themselves (Fig. 2).

The *p-spray* technique allowed the introduction of a punch-through bias grid, needed for sensor testing prior to connection to front-end electronics through bump-bonding. It consists of an implanted line running along every second column of pixels. The backside of the sensor has a multi guard ring structure to grade the potential, so that at the edge both sides are at about the same ground potential, in order to prevent sparking between detector and electronics. The dimensions of pixel cell are 50 μm × 400 μm.

Wafers containing two sensor *tiles* of the size to be used for ATLAS modules (16.4 × 60.8 mm^2) and several smaller sized sensors featuring the same active area (7.4 × 8.2 mm^2) as is covered by one front-end chip were fabricated in 200, 280 and 300 μm thicknesses by C.I.S. (Germany) and Seiko (Japan). One of the full-size tile designs had *p-stop* isolation structures, while the other used the *p-spray* technique. The smaller test

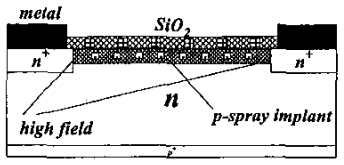

Figure 2: Schematic view of the implants in the p-spray insulation method. The charges inside the square boxes are fixed.

[1] Representing the ATLAS Pixel Collaboration[1]

[2] In what follows the doses are converted in n_{eq}/cm^2 where n_{eq} is the number of particles with the non-ionizing energy loss of a 1 MeV neutron [2, 3].

structures had various sensor designs, developed to study and optimise sensor performance in terms of inter-pixel capacitance, cross talk, noise, efficiency and intrinsic resolution. Some of these matched the tile designs and are known as ST1 (Single Tile 1) and ST2 (Single Tile 2) respectively. Fig. 3 and Fig. 4 show the layout of these designs in detail.

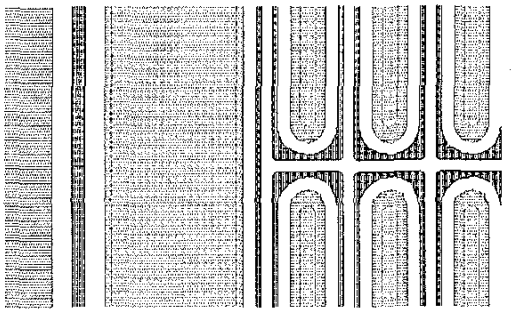

Figure 3: Details of the ST1 sensor design (*p-stop* isolation).

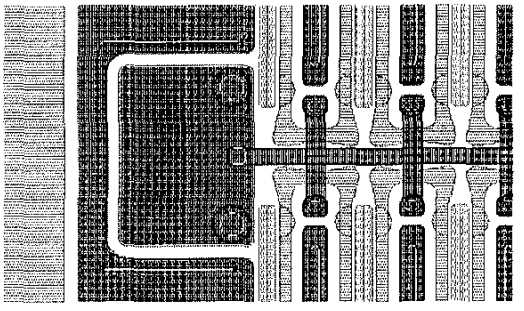

Figure 4: Details of the ST2 sensor design (*p-spray* isolation) in the region of the bias grid.

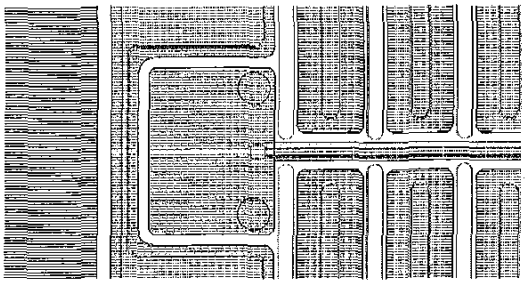

Figure 5: Details of the SSG sensor design (*p-spray* isolation) in the region of the bias grid.

In the ST1 design the p^+-type isolation rings surround the n^+-pixel implants. In the ST2 design there are also ring-like structures around each pixel but these are now n^+-type and were introduced to reduce the inter-pixel capacitance. A third design named SSG (Single Small Gap) is shown in Fig. 5. It uses *p-spray* isolation but does not include any intermediate n^+ structure. Neighbouring pixels have just small gaps between them. As will be shown in section II the ST2 design had a charge collection problem related to the presence of the floating atoll surrounding the pixel; for this reason SSG design was adopted as a baseline, after some modifications in the region of bias grid (SSGb design).

Front-end Electronics. In order to achieve the 40 MHz data acquisition rate needed at the high luminosity LHC, an end of column logic was adopted in the front end chip. It gathers the data out of the pixel column pairs (18 column of 160 rows per chip) and stores the valid information of a pixel hit (address, pulse amplitude, bunch crossing number) up to the time of the Level 1 trigger. If the event is subsequently selected by higher level triggers, the hit is read out from the front-end chip local buffers using the stored bunch crossing number. The pulse height measurement is performed by measuring the time the pulse from the amplifier remains above the threshold (Time Over Threshold). During the operation in the test beam the thresholds of the individual channels were adjusted, achieving a threshold dispersion of 170 electrons rms. Typical thresholds were around 3000 electrons, going down to 2000 electrons for charge collection studies. The noise was typically 150 electrons rms. The TOT was calibrated by injecting a known charge to every channel, with an accuracy of the order of 5 %.

Hybridization. In hybrid pixel technology, sensor and electronics chip are connected using bump and flip chip technology. Bump bonding at 50 μm pitch was considered a serious issue until recently. However several firms were able to provide high density bump bonding in both the Indium and PbSn solder technologies with a connection failure rate lower than 10^{-4}. For the Indium process, bumps are grown both on sensor and on electronics chip, while solder bumps are grown only on electronics surface, and flip chipping needs to be done at 250°C to re-flow the solder. Assemblies using both techniques were tested in the beam. No difference attributable to the bump bonding technique was found in their performance. For module hybridization two technologies are pursued: a flex-hybrid approach for discs and external barrel layers, while for the innermost barrel layer the MCMD (Multi Chip Module Deposited) technology will be adopted, providing bussing integrated on the detector surface (see dedicated talk by I.M.Gregor [7] at this conference).

B. *Irradiated Sensors*

To verify the radiation resistance of the sensor, some detectors were exposed to a flux comparable to those expected for LHC. Irradiations were performed using the 300 MeV/*c* pion beam at PSI and the 55 MeV/*c* proton beam at LBNL. Five sensors irradiated with fluences of 0.5×10^{15} and 1×10^{15} n_{eq}/cm^2 were tested in the beam. They were cooled at -9^0 C during data taking.

The two sensors with *p-stop* isolation (ST1) presented high noise even at low biasing voltages. This is understood to be due to high E-field at the boundaries of *p-stop* implants after bulk type inversion. On the contrary, irradiated sensors with *p-spray* separation were operated without excess current or noise at various voltages up to -600 V. The current was about 65 μA for a single chip sensor irradiated at 1×10^{15} n_{eq}/cm^2 and about 30 μA for one at 0.5×10^{15} n_{eq}/cm^2.

C. Test Beam Set-up

About 30 single chip assemblies and a few modules were characterized extensively in test beam experiments which were performed at the CERN SPS accelerator with a pion beam of 180 GeV/c momentum. A beam telescope consisting of 4 pairs of silicon microstrip detectors (each pair consisting of two planes of detectors with orthogonal strips) was used to measure the transverse position of the incident beam particles. The position resolution of tracks projected onto the test devices varied from 4.5 μm to 6.0 μm depending on the position of the detector under test with respect to the telescope. From the large variety of measurements made [8], only a few sensor-related results are discussed here.

II. Sensor-Related Test Beam Results

A. Charge Collection

The data were used to study the charge collection efficiency and uniformity for the various designs before and after irradiation. The capability of the readout chip to measure the charge collected by every pixel cell was essential for this study and the settings of the front-end electronics were optimised to allow an extended dynamic range for the charge measurement. For every particle crossing the detector, the cluster charge was calculated to take into account the charge sharing between adjacent pixel cells. The average cluster charge as a function

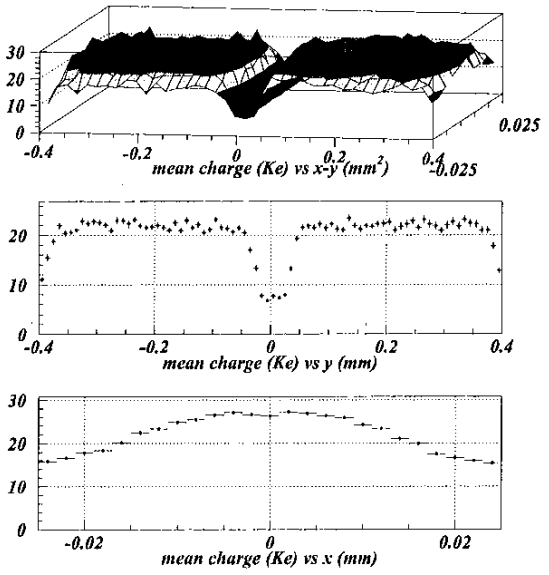

Figure 6: Average charge collected as a function of the position inside a pair of pixel cells for a 280 μm thick ST2 sensor.

of positions x and y inside a pair of pixel cells is shown in the upper plot of Fig. 6 for a 280 μm thick ST2 sensor. The coordinate axes are parallel to the short (50 μm) and the long (400 μm) edges of the pixels, respectively, and are centered (in x) at the center of a single pixel and (in y) between two adjacent pixels belonging to a column pair. The plots in the middle and at the bottom of the figure show the profile of the average cluster charge along the y axis (long pixel edge) and along the x axis (short edge) respectively. The average charge collected at the center of the pixel was $28 \cdot 10^3$ electrons; regions with reduced charge collection were observed for ST2 type sensors; these regions were located at the center of the plots in y or at the edges of the pixels in both x and y. A possible explanation [4] for this is that the n^+ implant ring that surrounds the main pixel implant (and which was introduced to minimize inter-pixel capacitance) did not float as it should, due to the presence of a current path not evident in the two-dimensional simulations used to optimize the design. It consequently collected signal charge, of which part was then lost due to capacitive coupling to parasitic nodes (e.g. the bias grid). (A study using three-dimensional simulation is in progress to understand this better.) At the end of each pixel directly adjacent to the bias grid, two charge loss effects combined: the capacitive effect described above and a direct loss to the implanted bias grid. In this region a relatively large amount of charge loss is visible, extending approximately $\pm$ 50 μm into the pixel region in the x direction; this loss profile corresponds roughly to the geometry of the bias structure. The first charge loss effect was absent from the SSG design, which had no n^+ implant ring. This design was then adopted as a baseline and was further modified in the region of the bias grid in order to reduce the second charge loss effect [9]. Results for this modified design known as SSGb show only a small charge collection inefficiency at alternate gaps, corresponding to the presence of the bias grid (Fig. 7 for a 200 μm thick modified SSG sensor. The lower level of signal was due to the smaller

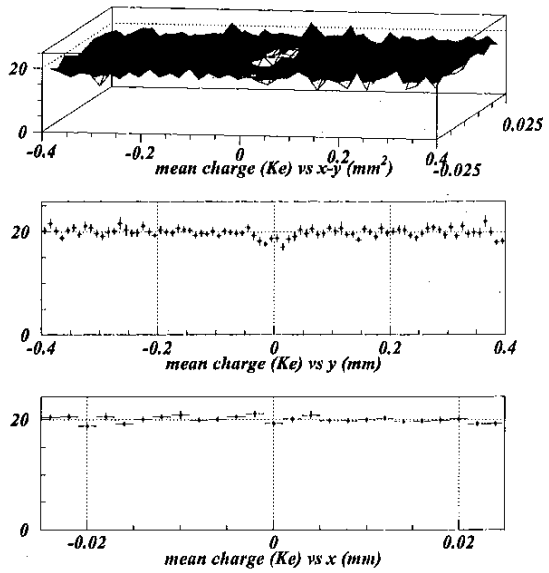

Figure 7: Average charge collected as a function of the position inside a pair of pixel cells for a 200 μm thick SSGb sensor.

sensor thickness). Sensors of ST1 type showed only a small charge collection inefficiency on all sides of each pixel due to

the presence of *p-stop* implants.

B. Charge Collection and Depleted Depth for Irradiated Sensors

As expected, after irradiation, the bulk material of our sensors underwent *type inversion*, becoming *p type*. As a consequence both of this and of the high concentration of radiation induced trapping centers, the full depletion voltage increased considerably and the sensors were only partially depleted, even when operated at biasing voltages of -600 V. In Fig. 8 the average cluster charge as a function of the

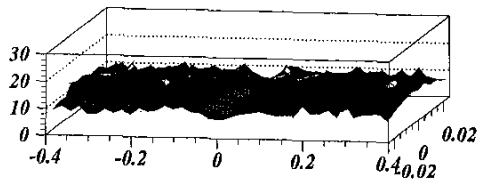

Figure 8: Average cluster charge as a function of the position inside a pair of pixel cells for a ST2 sensor after irradiation at a fluence of 10^{15} n_{eq}/cm^2.

beam particle position is shown for a ST2 sensor irradiated with a fluence of 10^{15} n_{eq}/cm^2. The charge losses at the edge of the pixel cells were similar to the not irradiated ST2 sensor, but the average charge collected at center of the pixel was $15 \cdot 10^3$ electrons. It was then interesting to measure the depletion depths of the two irradiated sensors. To perform this measurement, data were taken with the sensor at an angle $\geq 30^0$ with respect to the direction of the beam along the short direction of the pixel cells (Fig. 9). In this condition a beam

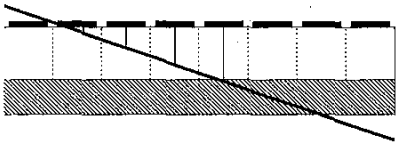

Figure 9: Illustration of the measurement of the depletion depth.

particle crossing the detector produced a cluster consisting of the pixel cells that had collected the charge of the subtended segment of the track. The depth of the center of each segment was calculated. The distribution of the depths is shown in Fig. 10 for three 280 μm thick sensors at different irradiations. From the distributions it was possible to measure the maximum depth at which the charge was still collected: a value of 187 $\pm$ 14 μm for the sensor irradiated at a fluence of 10^{15} n_{eq}/cm^2 was obtained. Since the thickness of the sensor was 280 μm , 68 $\pm$5 % of the charge should have been collected. Comparing this value with the 53% value actually measured, an upper limit of 20% charge trapping due to radiation damage can be assessed. A depletion depth of 265 $\pm$ 11 μm was measured for the sensor irradiated with 0.5×10^{15} n_{eq}/cm^2 when biased at -600 V. This measurement is consistent within the limits of error with a fully depleted detector.

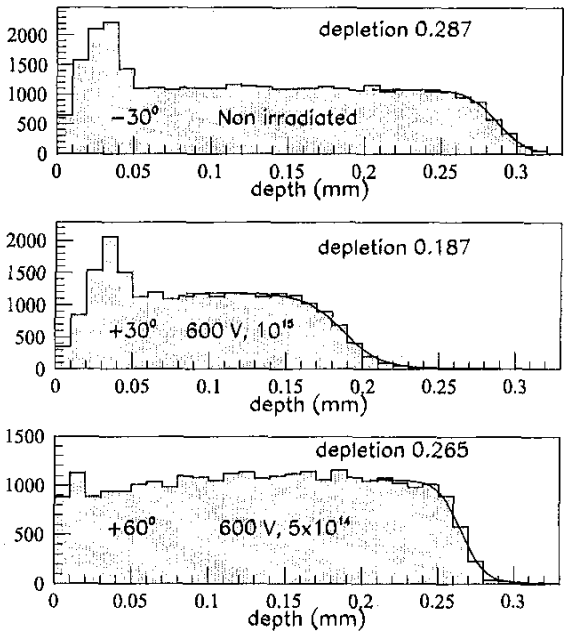

Figure 10: Distribution of the depth of the charge segments for a) a not irradiated fully depleted sensor; b) a sensor irradiated to a fluence of 10^{15} n_{eq}/cm^2 operated at -600 V reverse bias voltage; c) a sensor irradiated to a fluence of $0.5 \times 10^{15} n_{eq}/cm^2$, operated at -600 V reverse bias voltage.

C. Efficiency

With a 40 MHz bunch crossing rate expected at LHC, the charge collected by pixels must be detected in a time window of 25 ns. The in-time efficiency was determined by measuring the hit efficiency as a function of the arrival time of the particle. Since the extracted beams used at CERN did not have an RF structure and the readout electronics was operated with an asynchronous clock (with respect to the particles), the phase between the arrival time of every particle and the clock was measured [8]. Figure 11 shows the result obtained for the

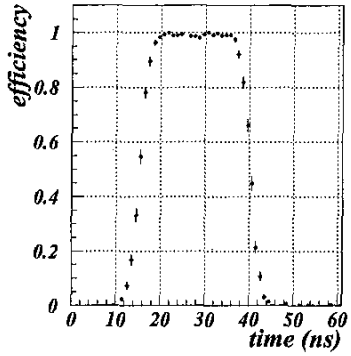

Figure 11: Efficiency versus time for a SSGb sensor.

modified p-spray sensors with a bias grid. A flat top of around

Table 1
Efficiency measurement summary.

Design	ST2	ST1	SSG	SSGb	ST2	ST2	ST2*
Isolation	p-spray	p-stop	p-spray	p-spray	p-spray	p-spray	
Fluence [n/cm^2]	0				5×10^{14}	10^{15}	
Bias [|V|]	150				600	600	
Depletion depth [μm]	full; 280			full; 200	265	187	
Thickness [μm]	280			200	280	280	
Threshold [Ke$^-$]	3.0				2.5	3.2	
Efficiency [%]	98.8	99.6	99.3	99.1	97.5	95.3	98.4
Losses [%]							
Total	1.2	0.4	0.7	0.9	2.5	4.7	1.6
No hits	0.4	0.1	0.2	0.4	1.3	2.2	0.4
Tracking	0.2	0.2	0.2	0.1	0.4	0.1	0.0
Timing	0.6	0.1	0.3	0.4	0.8	2.4	1.2
Cluster multiplicity [%]							
1 hit	82.0	72.0	71.7	81.8	71.0	86.3	94.2
2 hits	14.6	25.2	25.6	15.6	20.6	7.6	3.1
$\geq$ 3 hits	2.2	2.4	2.0	1.7	5.9	1.4	1.1

* with position cut, see text

16 ns is observed and an efficiency of 99.1% is measured.

In table 1 the overall efficiencies for various design sensors are summarised for thresholds of approximately 2Ke$^-$ and 3Ke$^-$. The efficiency losses reported in the table were due to three causes: missing hits, tracking errors in the silicon telescope or to the hits being out of time because of large time walk, which leads to assigning the hit to a successive bunch crossing w.r.t. the expected one (timing losses). For not irradiated sensors the values were at least equal to 99% in almost cases, except for ST2 at 3Ke$^-$ threshold which was 98.8%. This was due to the worse charge-collection efficiency mentioned above. For irradiated sensors it was found that a certain amount of losses were present, but confined to the regions with poor charge collection. Since there were no irradiated sensors of new design (without the charge loss) available at the time of the test beam, an estimate of their efficiency after full LHC irradiation was obtained using the data from the irradiated sensors of the first prototype, and requiring that the beam particle crossed the pixel inside a fiducial region in order to exclude the regions of poor charge collection. An efficiency of 98.4 % was obtained, with 1.2 % of hits out of time.

D. *Spatial Resolution*

Pixel spatial resolution is mainly determined by pixel cell size, by the choice between analog or digital readout and by the amount of charge sharing between adjacent pixels, the last one being determined both by sensor related parameters obtained by construction (inter pixel capacity, pixel capacity to the backplane) and operation (reverse bias operating voltage and irradiation, both influencing charge carriers diffusion) and by parameters related to electronic readout (threshold, noise, number of adc bits). A substantial role is also played by the incident particle track angle and by the $\vec{E} \times \vec{B}$ effect. If there is no charge sharing all the charge carriers locally generated around the incident particle trajectory are collected on a single pixel (single hit clusters) and spatial resolution is related to pixel size L by $\sigma = L/\sqrt{12}$. If the charge released by the passing particle is collected on neighbouring pixels (two or more pixel clusters), interpolation is possible, leading to improved resolution.

The charge sharing between adjacent pixels was studied using beam particles at normal incidence: for the 280 μm thick sensors, with a threshold of 3000 electrons, the region of charge sharing was extending for approximately $\pm$ 6 μm around the center of the two pixels; this region was reduced to approximately $\pm$ 4 μm for the 200 μm thick sensors.

In what follows, x is intended as the short (50 μm) and y as the long (400 μm) dimension of the pixel.

X-Spatial Resolution at Normal Incidence. The spatial resolution at normal incidence was measured by computing the residuals between the coordinate measured by the pixel detector and the one predicted by the silicon microstrip telescope. In fig. 12-14 the resulting distributions are shown for a SSGb 200 μm thick sensor. Single pixel and double pixel clusters were studied separately. For single pixel clusters the distribution was parametrized with a uniform distribution of width L, as discussed above, convoluted with a Gaussian distribution that took into account the resolution of the silicon strip telescope. The result of the fit gave L = 43.2 $\pm$ 0.2 μm for the extension of the region at the centre of the pixel where the charge was collected by a single pixel; the fitted width L was in agreement with the measured width of $\pm$ 4 μm of the region in which charge sharing occurs. Double pixel clusters were studied using two different algorithms: a *binary* algorithm that takes the average of the center positions of the two pixels, i.e. the center of the two hit pixels and an *analog* algorithm that corrects the binary position just described using the charge

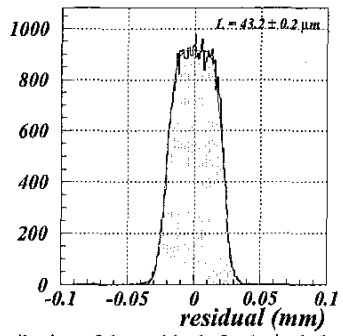

Figure 12: Distribution of the residuals for 1 pixel clusters.

collected by the two hit pixels.For the modified SSGb 200 μm thick sensor shown in Fig. 13 and Fig. 14 the width of the residuals calculated fitting the distributions with a Gaussian function gave 4.4 μm and 4.8 μm for the analog and digital algorithm respectively. For these measurements, the error on the predicted hit position was 4.2 μm, calculated taking into account the resolution of the silicon microstrip planes and the multiple scattering due to the material of the experimental set-up. The single pixel and double pixel cluster residuals were put together (Fig. 15). The rms of the overall distribution was 13.4 μm, determined by the relative fraction of single and multi-hit clusters and dominated by the single hit cluster resolution; subtracting the resolution of the silicon telescope, a value of 12.7 μm was obtained. The relative weight of the single pixel and double pixels clusters can be found in table 1.

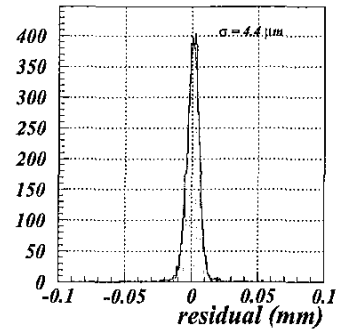

Figure 13: Distribution of the residuals for 2 pixels clusters using the analog algorithm (200 μm thick SSGb sensor).

X-Spatial Resolution as a function of Incidence Angle. Finally, the dependence of the resolution on the angle ϕ of the incident particle with respect to the normal to sensor was studied. For inclined tracks, the charge is collected over a region approximately given by $D \times tan(\phi)$, where D is the sensor depletion depth. Charged particles with large incident angle produce signals on many pixels and the average charge per pixel decreases, despite the longer trajectory in the silicon. Since only the signal amplitudes on the edge pixels in the clusters carry information on the position of the passing particle, the binary and the analog algorithms described above were used to reconstruct the coordinate but taking into account only the first and the last pixel in the clusters [10]. For each

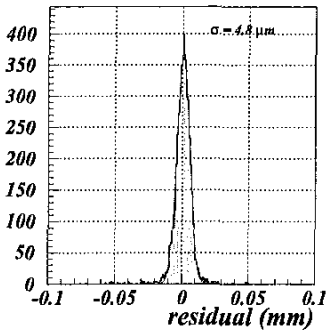

Figure 14: Distribution of the residuals for 2 pixels clusters using the binary algorithm (200 μm thick SSGb sensor).

angle of incidence of the track with respect to the normal to sensor, the rms of the overall residuals distribution was measured. The results are shown in Fig. 16 for a 280 μm thick SSG unirradiated sensor and for a sensor irradiated at a fluence of 10^{15} n_{eq}/cm^2. The data were not corrected for silicon strip telescope extrapolation error ($\approx$ 5μm, in these measurements). It can be noticed that as the angle increases the resolution first improves because of increased fraction of multi-hit clusters, taking advantage of charge sharing: at an angle of 10^0 the analog algorithm allows a resolution better than 6 μm to be obtained. The analog resolution degrades as the incident angle increases further, due to inefficiencies in the first and last pixel in the cluster, given the smaller amount of charge collected by each pixel. At most angles, analog algorithm provides a better spatial resolution. The minimum of the digital resolution at 5^o can be understood as follows; the best resolution is obtained when the fraction of single hit and double hit clusters are equal. This condition occurs when the projection on the pixel surface of the track segment inside the sensor matches the length of half pixel cell (25 μm). For a 280 μm thick sensor this condition is obtained at an angle of 5^o. More complicated figures occur at larger angles, when tracks leave signals on different numbers of pixels. Similar results were obtained for all the designs; given a design, no difference was found for different implant widths. The irradiated detector resolution never reaches values below 10 μm because of the small fraction of double pixel cluster (7.6 %). However this was a ST2 sensor, presenting the charge

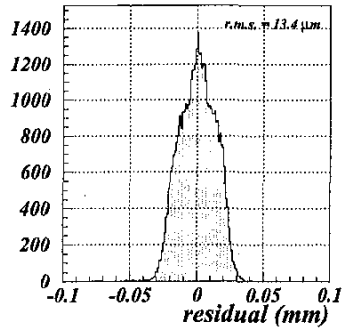

Figure 15: Distribution of the residuals for 1 pixel clusters and 2 pixels clusters using the binary algorithm.

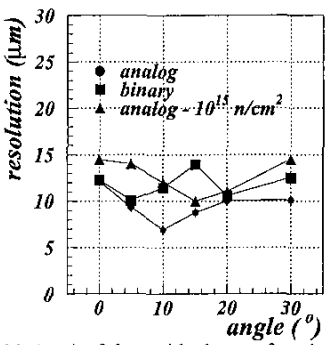

Figure 16: Width (rms) of the residuals as a function of the angle of incidence of the charged track w.r.t the normal to the sensor plane (280 μm thick sensors).

collection problems discussed above and an improvement is expected with new design sensors. It should also be noticed that the spatial resolution is not significantly degraded after irradiation: difference in spatial resolution before and after irradiation is fully explained in terms of reduced collected charge.

Y-Spatial Resolution. Charge sharing has no effect on the spatial resolution in the 400 μm long direction of the pixel given the limited region which it is restricted to. The corresponding y residuals present a flat distribution extending from $-200\mu m$ to $+200\mu m$ with an rms of $115\mu m$. In order to get a better y-resolution a bricked structure was designed and tested. This sensor had $400\mu m$ long pixels in adjacent columns displaced by $200\mu m$ in the long direction of the cell. With bricked design the same y-resolution just described is expected for single hit clusters while for multi-hit clusters the residual should have a flat distribution extending for half of this length with an rms of $58\mu m$. The overall resolution will then depend upon the fraction of clusters with 2 or more hits. The resolution was measured for angles ranging from 0^o to 30^o (Fig. 17). The fraction of clusters with ≥ 2 hits went from 46% at 0^o to 98% at 30^o, giving values of 65 - 67 μm for resolution between 10^o and 20^o. No variation of the x resolution was observed with respect to the non-bricked design.

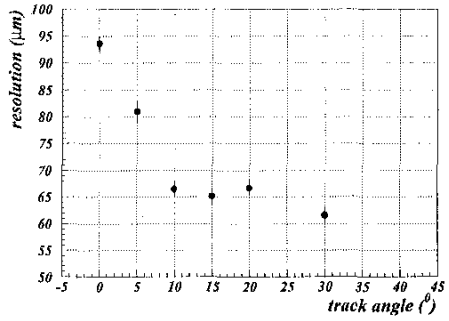

Figure 17: Resolution in the (400 μm) long direction of the pixel for a bricked design sensor as a function of the track angle of incidence with respect to the normal to sensor.

E. Lorentz Angle

As seen above, in the ATLAS experiment it is desirable to optimize the amount of charge sharing between pixels to optimize space resolution and efficiency. This will be done by tilting the sensors with respect to the beam line, but it should be taken into account that the ATLAS Pixel Detector will operate in a magnetic field of 2 tesla: in the barrel part of the detector, the magnetic field $\vec{B}$ and the electric drift field $\vec{E}$ inside the silicon pixel detector will be orthogonal and the drift velocity will have a component along the direction of $\vec{E} \times \vec{B}$. The charge carriers will then drift at an angle θ_L with respect to the direction of the electric field, θ_L being the Lorentz angle[11], such that $\tan\theta_L = \mu_H B$, where μ_H is the Hall mobility and B the magnetic field in tesla. Depending on the angle of the incident particle, the charge collected will spread over several pixels, the spread being minimum for an angle of the incident particle equal to θ_L. It is then important to measure the Lorentz angle of the sensors before and after irradiation, in order to define the best angle at which the barrel components of the Pixel Detector should be tilted. The method used to measure the Lorentz angle is well known [12]: the mean cluster size was measured as a function of the angle of the incident beam particles w.r.t. the normal to the detector. The Lorentz angle was given by the minimum of this distribution and was extracted from a fit to the data, where the fitting function was constructed using a model that had as input the results of our test beam measurements for charge sharing and depletion depth [8]. The mean cluster sizes as a function of the angle for a not irradiated sensor and one after 10^{15} n_{eq}/cm^2 irradiation are shown in Fig. 18; fits to data are also shown. The results

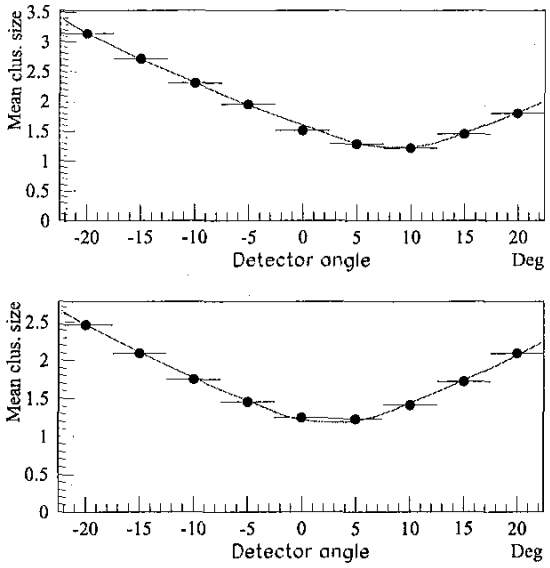

Figure 18: Mean cluster size as function of the track angle of incidence in a magnetic field of 1.4 T for a detector (top) not irradiated, (bottom) irradiated at 10^{15} n_{eq}/cm^2.

Table 2
Lorentz angle θ_L measurements

Fluence [n/cm^2]	0	5 x 10^{14}	5 x 10^{14}	10^{15}
Bias Voltage [|V|]	150	150	600	600
Depletion depth [μm]	280	125	265	190
θ_L[^{0}]	$9.1 \pm 0.1 \pm 0.6$	$5.9 \pm 1.0 \pm 0.3$	$3.0 \pm 0.5 \pm 0.2$	$3.2 \pm 1.2 \pm 0.5$

obtained are summarized in table 2 and presented a substantial decrease of θ_L after irradiation, when sensors were operated at -600 V. The Lorentz angle in a field of 1.4 tesla varied from $\theta_L = 9.1^0 \pm 0.1^0 \pm 0.6^0$ for a not irradiated sensor operated at -150 V to $\theta_L = 3.0^0 \pm 0.5^0 \pm 0.2^0$ for a sensor irradiated with 0.5×10^{15} n_{eq}/cm^2 and operated at -600 V and $\theta_L = 3.2^0 \pm 1.2^0 \pm 0.5^0$ for a sensor irradiated with 10^{15} n_{eq}/cm^2 and operated at -600 V, where the first error is statistical and the second one systematic. This behaviour can be understood (Fig. 19) as the result of a decrease of μ_H due to the variation of the electric field inside the sensor at the applied voltage and given by the modifications in depletion depth and space charge after irradiation. At high E the linearity between v_{drift} and E is no longer valid and saturation occurs.

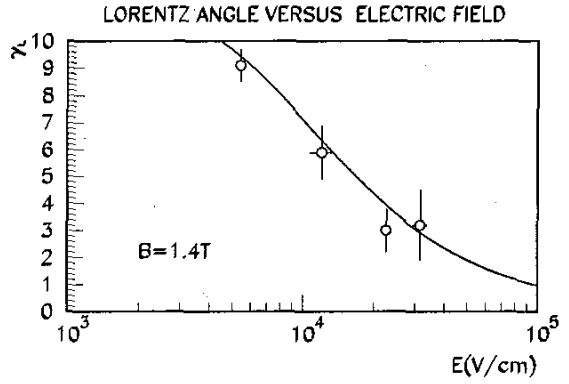

Figure 19: Measured Lorentz angle as a function of the electric field inside the sensor. The solid line represents the expectations given by the model.

III. Conclusions

About 30 single chip assemblies and a few module prototypes of the ATLAS Pixel Detector were tested in a beam with 40 MHz front-end electronics with analog readout. These measurements made it possible to check the overall feasibility of the project, to evaluate a series of prototype sensor designs and their radiation resistance, and to optimise the design and technological choices. It was shown that an efficiency greater than 99% and homogeneous charge collection can be achieved with the n^+ *in* n technology, both with *p-spray* and *p-stop* isolation, if a suitable design is used. The same performances were obtained with 200 μm thick sensors. Spatial resolution better that 6 μm was measured at 10° incident angle, taking advantage of charge sharing between pixels and of analog readout. It was also shown that *p-spray* sensors irradiated at the design fluence of 1×10^{15} 1 MeV $n_{eq} cm^{-2}$ were still operational, were depleted for 187 ± 14 μm at -600 V and provided a good in-time efficiency, without degradation in intrinsic resolution. An upper limit of 20% charge trapping due to radiation damage was measured. When operated in a magnetic field of 1.4 T at -600 V, the Lorentz angle was reduced by a factor 3 with respect to the value obtained at -150 V and before irradiation.

IV. Acknowledgements

The work reported here represents the joint efforts of many collegues in the ATLAS Pixel Collaboration. I would like to thank all of them.

V. References

[1] The ATLAS Pixel Collaboration, ATLAS Pixel Detector TDR, LHCC 98/13, CERN 1998.

[2] R. Wunstorf, IEEE Trans. on Nucl. Sci. 44(3) (1997) 806.

[3] H. Feick, Ph. D. thesis University Hamburg and DESY internal report F35D 97 08 (1997).

[4] The ATLAS Pixel Collaboration, "The ATLAS Silicon Pixel Sensors", Preprint CERN-EP (1999), submitted to Nucl. Instr. and Meth. A.
T. Rohe et al., Nucl. Instr. and Meth. A 409 (1998) 224.

[5] G. Batignani et al., Nucl. Instr. and Meth. A 277 (1989) 147.

[6] R.H. Richter et al., Nucl. Instr. and Meth. A 377 (1996) 412.

[7] O. Basken et al., NSS IEEE 99, to be published in IEEE Trans. on Nucl. Sci.

[8] F. Ragusa, "Recent Developments in the ATLAS Pixel Detector", 8th Internat. Workshop on Vertex Detectors, VERTEX 99, 20-25 June 1999, Texel, Netherlands, to be published on Nucl. Instr. and Meth. A.

[9] T. Rohe, PHD Thesis, Ludwig Maximilians Universitat, Munich, 1999.

[10] C. Troncon, "Measurement of spatial resolution and charge collection in double sided double metal silicon microstrip detectors",Nuclear Physics B, 44 (1995) 287
R. Turchetta, Nucl. Instr. Meth. A 335 (1993) 44.

[11] S.R. Amendolia et al., Nucl. Instr. and Meth. A 235 (1985) 296.

[12] E. Belau et al., Nucl. Instr. and Meth. A 214 (1983) 214.
N. Bingefors et al., Nucl. Instr. and Meth. A 328 (1993) 447.